View metadata, citation and similar papers at core.ac.uk
brought to you by CORE
provided by NASA Technical Reports S

AAS 15-224

SUPERSONIC FLIGHT DYNAMICS TEST: TRAJECTORY, ATMOSPHERE, AND AERODYNAMICS RECONSTRUCTION

Prasad Kutty*, Christopher D. Karlgaard†, Eric M. Blood‡, Clara O'Farrell§, Jason M. Ginn¶, Mark Schoenenberger‖, Soumyo Dutta**

The Supersonic Flight Dynamics Test is a full-scale flight test of a Supersonic Inflatable Aerodynamic Decelerator, which is part of the Low Density Supersonic Decelerator technology development project. The purpose of the project is to develop and mature aerodynamic decelerator technologies for landing large mass payloads on the surface of Mars. The technologies include a Supersonic Inflatable Aerodynamic Decelerator and Supersonic Parachutes. The first Supersonic Flight Dynamics Test occurred on June 28th, 2014 at the Pacific Missile Range Facility. This test was used to validate the test architecture for future missions. The flight was a success and, in addition, was able to acquire data on the aerodynamic performance of the supersonic inflatable decelerator. This paper describes the instrumentation, analysis techniques, and acquired flight test data utilized to reconstruct the vehicle trajectory, atmosphere, and aerodynamics. The results of the reconstruction show significantly higher lofting of the trajectory, which can partially be explained by off-nominal booster motor performance. The reconstructed vehicle force and moment coefficients fall well within pre-flight predictions. A parameter identification analysis indicates that the vehicle displayed greater aerodynamic static stability than seen in pre-flight computational predictions and ballistic range tests.

INTRODUCTION

The Low Density Supersonic Decelerator (LDSD) project is a NASA technology development program designed to mature aerodynamic decelerator technologies that can be used for landing high mass payloads (beyond the present capability of Viking-derived 70-degree sphere cone entry vehicles) on the surface of Mars.[1] Through a series of extensive ground and flight tests, the following decelerator technologies will be developed: a Supersonic Inflatable Decelerator for Robotic missions (SIAD-R),[2] a Supersonic Inflatable Decelerator for Human Exploration missions (SIAD-E),[3] and a supersonic parachute.[4] The flight test campaign, referred to as the Supersonic Flight Dynamics Test (SFDT),[5] will exercise the decelerator technologies with three full scale, high-altitude missions at the Pacific Missile Range Facility (PMRF) in Kauai, Hawaii. The first of these tests, SFDT-1, was conducted on June 28, 2014. Two remaining flight tests, SFDT-2 and SFDT-3, are scheduled to be completed during the summer of 2015.

The SFDT Test Vehicle (TV) configuration is shown in Figure 1. The TV is a 4.7 m diameter aeroshell with a spherical forebody similar in shape to the Apollo command module, with a shoulder radius equivalent to the Mars Science Laboratory entry capsule. The SFDT TV forebody is designed to match the shape of a Mars Design Reference Vehicle (DRV).[6] The SFDT TV outer mold line matches that of the DRV forward of the backshell-heatshield separation plane. The SFDT capsule backshell is removed to accommodate a STAR-48 solid rocket motor and a camera mast. The SIAD-R is a 6 m diameter attached torus. The SIAD-R deployed configuration is shown in Figure 1(b).

The nominal SFDT-1 flight sequence is illustrated in Figure 2. The sequence begins with the launch of the balloon-carried test vehicle (TV) from the ground. The balloon carries the TV to an altitude of approximately

*Project Engineer, Analytical Mechanics Associates, Inc., Hampton, VA.
†Supervising Engineer, Analytical Mechanics Associates, Inc., Hampton, VA. Member AAS, Senior Member AIAA.
‡Systems Engineer, EDL and Advanced Technologies, Jet Propulsion Laboratory, California Institute of Technology, Pasadena, CA.
§Guidance and Control Engineer, EDL Guidance and Control Systems, Jet Propulsion Laboratory, California Institute of Technology, Pasadena, CA.
¶Summer Intern, EDL and Advanced Technologies, Jet Propulsion Laboratory, California Institute of Technology, Pasadena, CA. Currently Graduate Student, Georgia Institute of Technology.
‖Aerospace Engineer, Atmospheric Flight and Entry Systems Branch, NASA Langley Research Center, Hampton, VA. Senior Member AIAA
**Aerospace Engineer, Atmospheric Flight and Entry Systems Branch, NASA Langley Research Center, Hampton, VA. Member AIAA.

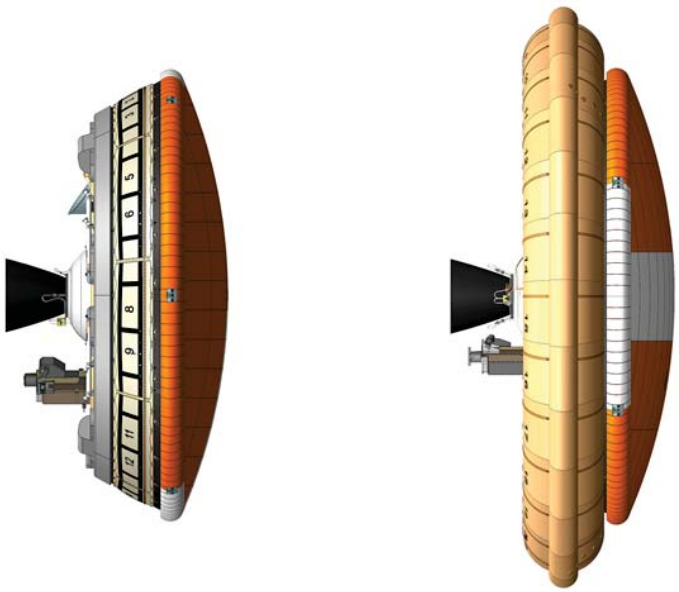

(a) SFDT Powered Flight and Coast Phase Configuration

(b) SFDT SIAD-R Test Phase Configuration

Figure 1: SFDT Test Vehicle Configuration

120,000 ft. The TV is released from the balloon, spin-up motors fire, and a STAR-48 solid rocket motor ignites to carry the vehicle to the desired test condition of 180,000 ft and Mach 4. After the motor burn is complete, the vehicle is de-spun. Upon reaching a pre-determined planet-relative velocity, the onboard computer commands the deployment of the SIAD, which begins the test period of the mission. The vehicle decelerates to a condition of Mach 2.5 where the Parachute Deployment Device (PDD) is deployed, extracting the main parachute. The TV remains under the Supersonic Disksail Parachute (SSDS) for the remainder of the flight until landing in the Pacific Ocean. The TV, Flight Imagery Recorder (FIR), PDD, SSDS, balloon carcass and recovery parachute were all recovered after the flight at the location of 23.398560° N, -160.152078° E.

The primary objective of SFDT-1 was to validate the test architecture as a platform for demonstrating the technology under development for LDSD by delivering the TV to the targeted flight conditions. The main goals of the flight were to demonstrate stable powered flight and correct triggering of events by the flight computer. These goals were successfully met for SFDT-1, proving an effective test design for the upcoming SFDT-2 and SFDT-3 missions through which the decelerator technologies can be tested. It should be noted that the SIAD was successfully demonstrated for SFDT-1, while the SSDS suffered a structural failure and did not properly deploy. However, nominal performance of these technologies was not a requirement for SFDT-1 and any knowledge of these systems gained through the first flight test was considered an additional benefit.

This paper describes the data sources and methodology used to reconstruct the SFDT-1 trajectory, atmosphere and aerodynamics. The remainder of the paper is organized as follows. A summary of the sensor measurements available for use in the reconstruction is given and the quality of the measurements from the test flight is described. An overview of the reconstruction methodology and tools is presented. Results of the reconstruction are shown and explored.

INSTRUMENTATION AND MEASUREMENTS

A variety of measurement sources were available for use in the trajectory and atmosphere reconstruction process. These measurements included onboard instrumentation such as an Inertial Measurement Unit (IMU) and Global Positioning System (GPS), ground-based measurements from tracking radars, and atmospheric soundings from balloons and high altitude rockets. The following sections provide a more detailed overview of the measurement sources and their performance on the day of flight.

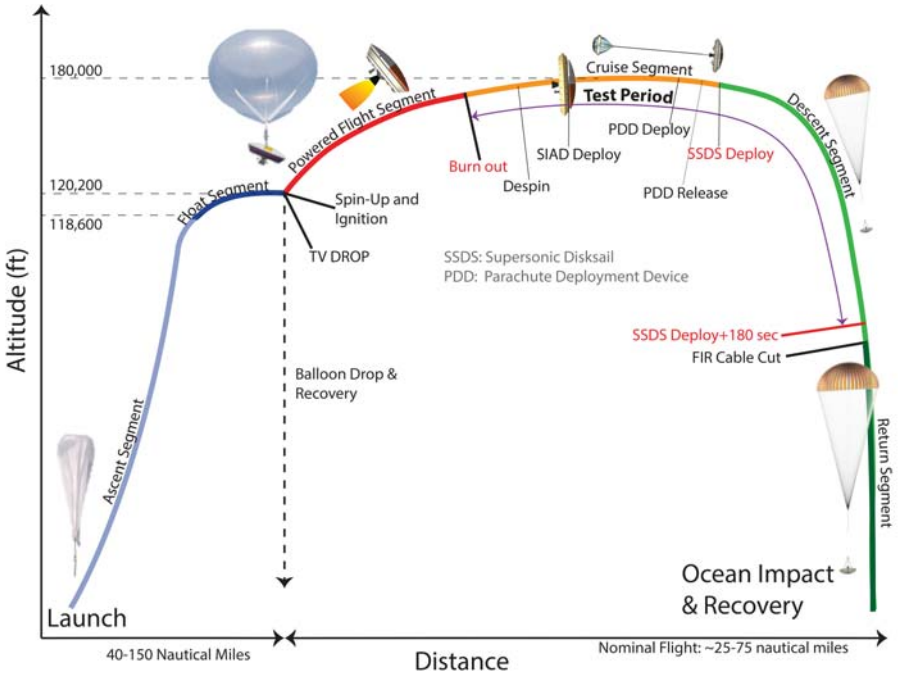

Figure 2: Supersonic Flight Dynamics Test One Overview

Inertial Measurement Unit

Three-axis linear accelerations and angular rates were measured by a Gimbaled LN-200 with Miniature Airborne Computer (GLN-MAC) inertial navigation system. The LN-200 inertial measurement unit contains three-axis solid-state silicon Micro Electro-Mechanical System (MEMS) accelerometers and three-axis solid-state fiber-optic gyroscopes. The GLN-MAC incorporates a roll isolation gimbal to produce a stable platform for spinning vehicle applications. An electric motor is used to counter-rotate the internal mount plate such that the LN-200 senses a low rotational rate about the roll axis. The gimbaling has the effect of reducing error buildup due to scale factor uncertainties in the roll gyro. The angle of the mount plate is measured with a resolver. The GLN-MAC is mounted in the vehicle approximately 0.5 m off the centerline. The GLN-MAC has the capability to "cage" or lock the LN-200 in a preferred orientation, creating a true strapdown IMU. This mode was not used for the SFDT-1 flight; the LN-200 was free to gimbal throughout the entire flight test.

The GLN-MAC produces two sets of telemetry, one from the gimbaled LN-200 at a rate of 400 Hz and one from the integrated GLN-MAC system at a rate of 100 Hz. The resolver angle is also telemetered at a rate of 400 Hz. The GLN-MAC level outputs utilize the resolver angle and resolver rate to generate an equivalent strapdown representation of the gimbaled LN-200 accelerations and rates. Typical performance characteristics of the GLN-MAC sensor can be found in Reference 7. The particular unit used onboard the SFDT-1 flight was thoroughly tested and evaluated, and the reconstruction assumptions were tuned to match the observed performance characteristics of the device (noise and misalignments). The raw LN-200 data was corrected post-flight for known thermal biases and misalignments prior to its use in the trajectory reconstruction. The data quality was good with the exception of a loss of a single 100 Hz frame during powered flight at a time approximately 45.7 s after drop from the balloon.

Global Positioning System

Measurements of position and velocity were obtained from a Javad G2T GPS receiver at a rate of 10 Hz. The GPS antennas were located in a diametrically opposed configuration on the shoulder of the vehicle. A pre-flight analysis of the SFDT-1 trajectory determined that the GPS receiver would loose lock on the satellites during powered flight due to the high spin rate experienced by the vehicle. As expected, a GPS dropout was observed between spin up and vehicle spin down. The GPS receiver reacquired satellites nominally and provided valid measurements through the remainder of the trajectory.

The Javad unit also produced estimates of the uncertainties in the position and velocity solution based

on the number of satellites in view, shown in Figure 3(a), and the covariance of the onboard solution. The receiver estimates of position and velocity RMS errors are shown in Figure 3(b).

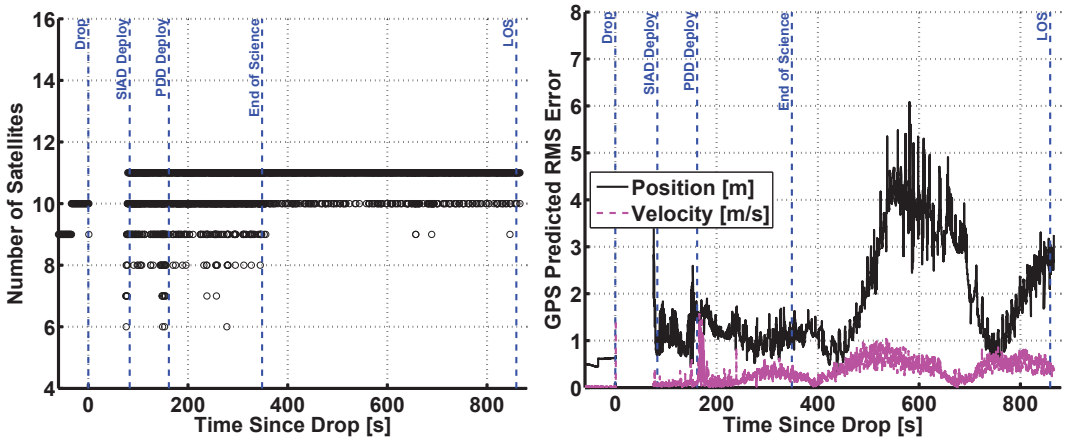

(a) Number of Satellites

(b) GPS Solution RMS Error

Figure 3: GPS Satellites and RMS Errors

Tracking Radar

Range, azimuth, and elevation measurements of the test vehicle were provided by three ground-based C-Band tracking radars operated by PMRF. Two tracks, referred to as Q8 and Q9, were provided by beacon tracking Radar Open System Architecture (ROSA) radars at a rate of 40 Hz. One track, referred to as Q4, was provided by a wide-band/narrow-band skin tracking Digital-Receiver Coherent Signal Processor (DR-COSIP) radar at a rate of 10 Hz. The locations of these radars relative to the as-flown trajectory are shown in Figure 4 and information on the radars is given in Table 1. The C-Band radar beacons were mounted in a diametrically opposed configuration on the shoulder of the vehicle.

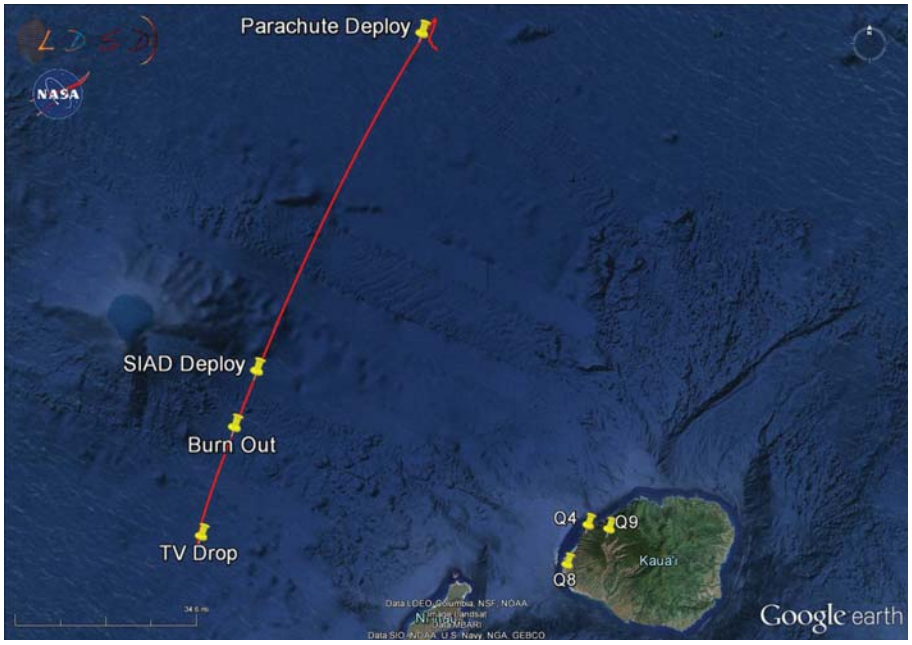

Figure 4: SFDT-1 Ground Track and Radar Locations

In general, the measured radar tracks were of good quality and were in overall agreement. Based on recommendations from PMRF, the wide-band data from Q4 was chosen because of lower noise and systematic

Table 1: Radar Stations

Radar	Architecture	Type	Site	Time Spans (seconds since drop)
Queen 4	DR-COSIP	AN/FPQ-19	Makaha Ridge	-60-0, 30-440
Queen 8	ROSA	AN/MPS-25	Barking Sands	-60-200
Queen 9	ROSA	AN/MPS-25	Kokee Park	0-200

error content than the narrow-band track.

Meteorological Data

Meteorological sounding rockets and weather balloons were used to obtain the atmospheric characteristics through which the vehicle flew during SFDT-1. The rocket sounding was performed by a 1 m diameter mylar PWN12A Rocket Balloon Instrument (ROBIN) sphere that was launched by a Super Loki rocket. The ROBIN sphere was deployed at apogee, and tracked by radar during descent. The sphere fell until it reached an altitude of 25-30 km where it collapsed due to the ambient pressure. With known drag characteristics, the atmospheric density and winds were estimated from the radar track.

Each weather balloon carried a Vaisala RS-92 radiosonde. The RS-92 contained a capacitive wire temperature sensor, a Barocap silicon capacitive pressure sensor, a thin-film capacitive humidity sensor, and a GPS receiver. The atmospheric pressure profile was estimated from the pressure sensor directly, or from the temperature measurements combined with GPS altitude and the hydrostatic equation. Winds were derived using the GPS measurements.

In total, six balloons and four rocket launches were performed for the SFDT-1 flight. The timeline of launches is shown in Table 2. Two of the rocket launches failed to deploy the ROBIN sphere correctly, providing no data. The third rocket deployed nominally and was adequately tracked by radar allowing recovery of the atmosphere profile. The fourth rocket deployed the ROBIN sphere, but collapsed prematurely such that a partial profile consisting of only winds could be recovered.

Table 2: SFDT-1 Atmospheric Measurement Timeline with Significant Events in Bold

Time (HST)	Event
3:00	Weather balloon 1 launched
3:59	Weather balloon 2 launched
4:24	Weather balloon 3 launched
7:23	Weather balloon 4 launched
7:48	Weather balloon 5 launched
8:45	**SFDT Liftoff**
10:12	Weather balloon 6 launched
10:35	Sounding rocket 1 launched (failure)
11:05	**SFDT drop**
11:35	**SFDT splashdown**
12:08	Sounding rocket 2 launched (failure)
12:38	Sounding rocket 3 launched
13:25	Sounding rocket 4 launched (partial failure)

Of the six balloons launched, only data from the sixth balloon were incorporated into the atmospheric reconstruction. This balloon was chosen because the measurement time was closest to the time of the SFDT flight operations. This balloon was launched at 10:12 HST and ascended to its maximum altitude of approximately 33.3 km over a period of 42 minutes. Therefore, the measurements at maximum altitude occurred 13 minutes before the SFDT test vehicle was dropped from its balloon.

RECONSTRUCTION METHODS

The instrumentation utilized during the SFDT-1 mission provided an incredibly rich set of measurement data from which reconstruction was performed. The following section describes the methodologies used to reconstruct the trajectory, atmosphere and aerodynamics given the measurements taken during flight.

Atmosphere Reconstruction

Upper atmosphere characterization was achieved from a combination of the Super Loki rocket with PWN12A ROBIN sphere payload, anchored to atmospheric conditions in the lower atmosphere based on radiosonde data. The density and winds were determined using the radar tracking data, assuming known drag coefficient, pressure at the lowest altitude (based on radiosonde), and an initial guess of the atmospheric density profile. For this work, the Mass Spectrometer and Incoherent Scatter (MSIS-E-90) atmosphere profile[8] was used as the initial guess for the density profile.

The ROBIN sphere data provided an incremental density profile relative to the assumed initial density profile. The incremental density was then anchored to the radiosonde data at the lowest ROBIN Sphere altitude (referred to as the *tie-on altitude*) to produce accurate density values. For this process, temperatures were derived from the ROBIN sphere density profile by assuming the atmosphere was in a state of hydrostatic equilibrium. The assumption of a hydrostatic atmosphere below the tie-on altitude also enabled the use of the GPS altitude measurements and the radiosonde capacitive wire temperatures measurements to produce a static pressure profile that was more precise than that given by the Barocap pressure sensor. The density profile was then computed from the temperature profile and hydrostatic pressure profile using the equation of state. Thus, the combination of radiosonde temperature and GPS altitude with ROBIN sphere temperature and radar tracking data produced a self-consistent atmosphere that satisfied the equation of hydrostatic equilibrium and the equation of state.

Trajectory Reconstruction

The SFDT-1 trajectory reconstruction was performed using a Matlab-based Iterative Extended Kalman Filter (IEKF)[9] code known as NewSTEP. This software is a generalization of the Statistical Trajectory Estimation Program (STEP)[10,11] that was developed by NASA Langley Research Center and applied to launch and entry vehicle trajectory reconstruction analyses during the 1960s-1980s. The NewSTEP code borrows largely from STEP, but includes various enhancements to the core code that have been developed to accommodate the reconstruction needs of recent flight projects.[12–17,19] Some of the more important enhancements implemented in the NewSTEP software include the iterative Kalman filter capability, the addition of new measurement sources and output parameters, and improved methods of internal state covariance transformation used to obtain output uncertainties.

The IEKF is a widely used method for state estimation and trajectory reconstruction that optimally blends all of the available measurement data relating to the vehicle trajectory. The algorithm is a predictor/corrector in which state predictions are computed from numerical integration of the rigid-body equations of motion, and corrections to the state estimate are computed from a weighted least-squares fit of the state to the observed data. The forward pass of the filter processes the data from the initial time to the final time, propagating through all of the observed data. Since only the end point of the forward pass will have benefited from all available measurement data, a backward pass is utilized that propagates the state estimate from the final time back to the initial time point. These two passes are merged using the Fraser-Potter smoothing algorithm, so that each data point in the reconstructed trajectory is estimated from all available data.

Lastly, output transformations are made to generate estimates of quantities of interest, such as Mach number and dynamic pressure, which are not internal state variables estimated in the Kalman filter. This is effectively a post-processing step outside of the IEKF algorithm in which output parameters are computed and uncertainty transformations are performed that map the internal state variances into output uncertainties.

Several modifications were made to the core code to accommodate unique inputs and outputs for SFDT-1. The most significant of these modifications was an improved post-processing model used to handle the IMU measurements, which were complicated by the presence of the gimbaled system. Many past applications of gimbaled IMU reconstructions have made use of an equivalent strapdown representation of the linear accelerations and angular rates in the estimation filter by transforming the platform data into a strapdown frame via the measured gimbal angle.[16,20] This approach has the advantage of producing a strapdown representation of the inertial measurements without any error buildup due to roll gyro scale factor. The drawback to this method is that resolver angular rate and acceleration uncertainty will degrade the measurements substantially due to resolver angle quantization, amplified by errors from numerical differentiation.

For the SFDT-1 reconstruction, an alternate approach was devised in which the trajectory of the LN-200 itself was reconstructed from the measurement data using the Kalman filter approach to blend IMU

measurements with GPS and Radar. The output of this process is a kinematic reconstructed trajectory of the LN-200 in an IMU-relative frame through inertial space. After reconstructing the LN-200 trajectory, the resolver angle profile is used to transform the state outputs into the vehicle aerodynamic coordinate frame as shown in Figure 5. Additionally, the reconstructed mass properties are incorporated in order to translate the reconstructed state of the vehicle to the center of gravity (CG).

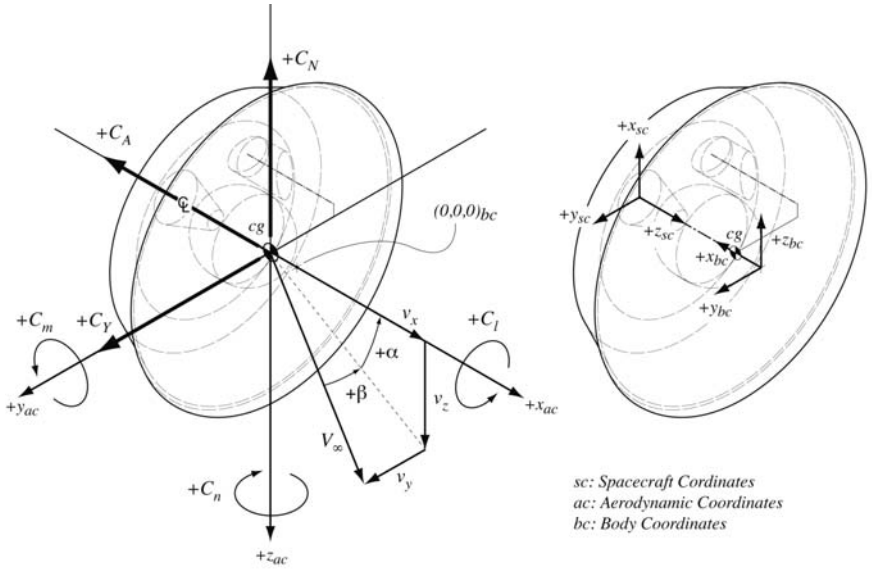

Figure 5: Test Vehicle Flight Dynamics Coordinate Frames

At this point in the process, the resolver quantization uncertainty corrupts the reconstructed vehicle state, but this uncertainty is an algebraic mapping at each instant in time such that the resolver angle uncertainties do not propagate over time. After transforming the LN-200 state to the vehicle body frame at the CG, the freestream atmosphere is computed as a function of altitude from a table lookup, and the atmospheric relative state (angle of attack, Mach number, dynamic pressure, etc.) and vehicle aerodynamics are computed.

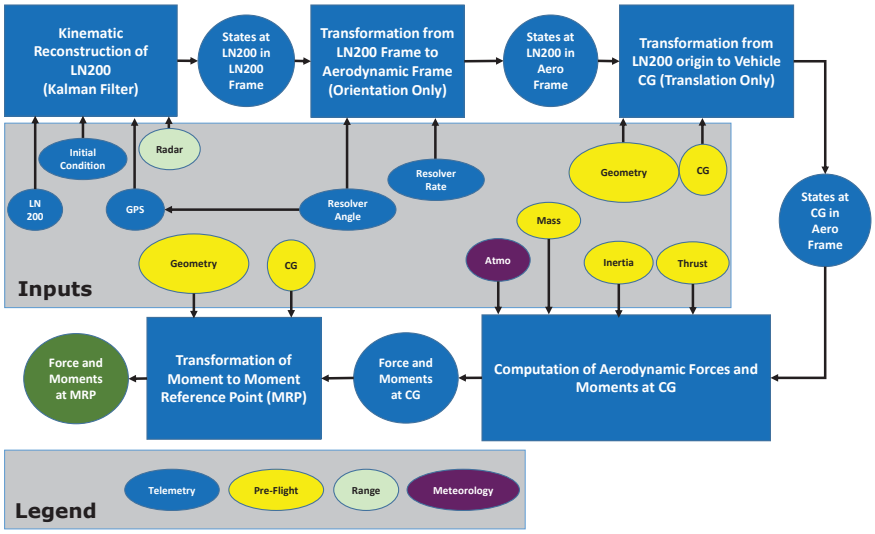

Figure 6: Reconstruction Flow

A flow diagram of the overall trajectory reconstruction process is shown in Figure 6. The process begins with the kinematic reconstruction of the LN-200 based on the Kalman filter solution that blends the IMU

accelerations and rates, GPS position and velocity, initial conditions, and ground-based radar tracking.

Mass Properties Generation

Reconstructed mass properties were used to calculate the aerodynamic parameters of the vehicle as well as output state variables (including accelerations and angular rates) at the CG. Instrumentation to measure the vehicle mass properties was not utilized for SFDT-1, requiring their values to be determined using pre-flight models and measured event times. Specifically, the flight dynamics simulation, POST2 (Program to Optimize Simulated Trajectories II), which was used as a pre-flight predictor of the vehicle performance,[21] was also used to model the post-flight trajectory and mass property history of the TV.

Using observed events during SFDT-1, the POST2 simulation was adjusted to represent the as-flown timeline in generating the mass, reference area, CG location, moments of inertia and products of inertia of the TV. For example, the burnout detection mode of the vehicle flight software was triggered when sensed axial acceleration reached a value of zero, indicating that aerodynamic drag was equal to axial thrust. From this observed event, the thrust and corresponding mass history in the simulation could be adjusted to provide a reconstructed mass profile. Similar flight observables, such as the time of SIAD deployment, PDD deployment, and SSDS line stretch allowed for the adjustment of the pre-flight mass history for reconstruction.

Aerodynamics Reconstruction

The vehicle aerodynamic force and moment coefficients were calculated from the linear and angular accelerations (after transformation from the LN-200 to the vehicle aerodynamic frame), reconstructed dynamic pressure, vehicle mass, reference area, and length by means of the equations*

$$\left\{ \begin{array}{c} C_A \\ C_Y \\ C_N \end{array} \right\} = -\frac{m}{Sq}\left(\boldsymbol{a} - \boldsymbol{T}/m\right) \tag{1}$$

$$\left\{ \begin{array}{c} C_l \\ C_m \\ C_n \end{array} \right\} = \frac{1}{Sqd}\left(\mathcal{I}\dot{\boldsymbol{\omega}} + \boldsymbol{\omega} \times \mathcal{I}\boldsymbol{\omega}\right) \tag{2}$$

where the quantity $\boldsymbol{T}$ represents the STAR-48 solid rocket motor thrust profile.

Aerodynamic parameter identification techniques were utilized to estimate vehicle trim characteristics and stability derivatives. The approach utilized here follows the methodology developed for capsule aerodynamic parameter identification for Mars Science Laboratory,[22,23] with the exception that the SFDT-1 trim angle of attack was zero degrees. The stability derivatives were extracted from the linearized longitudinal and lateral/directional capsule dynamics.

The linearized longitudinal model (neglecting heaving) is of the form

$$\left\{ \begin{array}{c} \dot{\alpha} \\ \dot{\omega}_y \end{array} \right\} = \left[\begin{array}{cc} (\partial\dot{\alpha}/\partial\alpha) & (\partial\dot{\alpha}/\partial\omega_y) \\ (\partial\dot{\omega}_y/\partial\alpha) & (\partial\dot{\omega}_y/\partial\omega_y) \end{array} \right] \left\{ \begin{array}{c} \alpha \\ \omega_y \end{array} \right\} \approx \left[\begin{array}{cc} 0 & 1 \\ SqdC_{m_\alpha}/\mathcal{I}_{yy} & 0 \end{array} \right] \left\{ \begin{array}{c} \alpha \\ \omega_y \end{array} \right\} \tag{3}$$

The solution takes the form of a phase-shifted sinusoid, $\alpha = A\cos\left(\Omega_y t + \delta\right)$ where A and δ are constants of integration, and Ω_y is the natural frequency, which can be found from the roots of the characteristic equation to be

$$\Omega_y = \sqrt{-\frac{Sqd}{\mathcal{I}_{yy}}C_{m_\alpha}} \tag{4}$$

The frequency of oscillation can be estimated from either the reconstructed vehicle attitude or measured pitch rate by fitting either signal to an analytic expression of a sinusoid function from which the frequency, Ω_y, can be easily obtained. Then, the pitch stability derivative can be computed as:

$$C_{m_\alpha} = -\frac{\mathcal{I}_{yy}\Omega_y^2}{Sqd} \tag{5}$$

Similarly, the linearized lateral-directional capsule dynamics yields an expression for the yaw stability derivative of the form

$$C_{n_\beta} = \frac{\mathcal{I}_{zz}\Omega_z^2}{Sqd} \tag{6}$$

*All of the mathematical symbols used are listed in the Notation section at the end of the paper.

Note that Eq. (6) assumes a zero trim angle of attack. The analysis becomes more complicated for nonzero trim angles, as described in Reference 23.

Over one brief segment of the data the mean pitch-damping coefficient was extracted using the angle of attack history for a qualitative comparison. As shown in Reference 24, the aerodynamic moments acting on a decelerating blunt body take the form of the Euler-Cauchy (EC) equation. This equation has an analytic solution that can be used to identify an effective pitch damping. To get an analytic solution to the moment equation, one must assume planar motion, constant density, and constant drag and damping coefficients. The SFDT-1 results for both static and dynamic stability will be presented in the following section.

FLIGHT DATA ANALYSIS

This section describes the application of the methods described in the previous section to the reconstruction of the trajectory, atmosphere, and aerodynamics of the SFDT-1 test vehicle.

Reconstructed Atmosphere

Figures 7 and 8 show the reconstructed atmosphere profile based on the PWN12A ROBIN sphere measurements and the RS-92 radiosonde. For comparison, the atmosphere based on the Earth Global Reference Atmosphere Model (GRAM)[25] is also shown. The altitudes of several important events along the reconstructed SFDT-1 flight path are indicated. For the altitudes corresponding to the SFDT-1 flight path, the reconstructed atmospheric density was roughly 1-2 standard deviations below the nominal GRAM profile. The temperature profile is fairly consistent with the nominal GRAM atmosphere, but the data does show a prominent double stratopause in the region of 45-55 km altitude. Previous studies of double stratopause occurrences suggest that this phenomenon occurs at a rate of roughly 45% in the summer months.[26] It is therefore reasonable that this double stratopause is realistic and not the product of measurement uncertainties. Note that the atmospheric density and pressure profile were based solely on data from weather balloon 6 and sounding rocket 3.

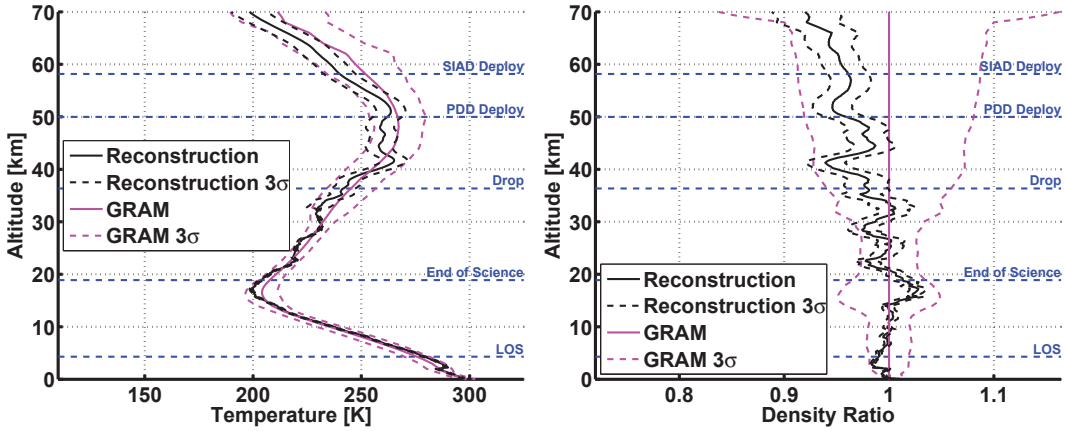

(a) Freestream Temperature

(b) Freestream Density

Figure 7: Reconstructed Atmosphere States

The reconstructed horizontal winds were based on a combination of sounding rockets 3 and 4. Although rocket 4 collapsed prematurely (producing unreliable density and temperature profiles due to uncertainty in drag coefficient), wind estimates were still obtained from the radar track of the deflated sphere. A weighted averaging was used such that the profile from rocket 4 received half the weight of the profile from rocket 3. This weighting was based on engineering judgement to give more weight to the rocket closest to the time of the SFDT-1 flight[†].

It is important to note that the uncertainties of the atmospheric reconstruction are based solely on instrumentation error specifications and do not include estimates of any potential spatial or temporal perturbations that may occur due to wind gusts or density pockets. There is no indication from other SFDT-1 flight data that any such perturbation was encountered during the flight test.

[†]The sounding rocket wind profiles were provided to the reconstruction team by the range meteorology group.

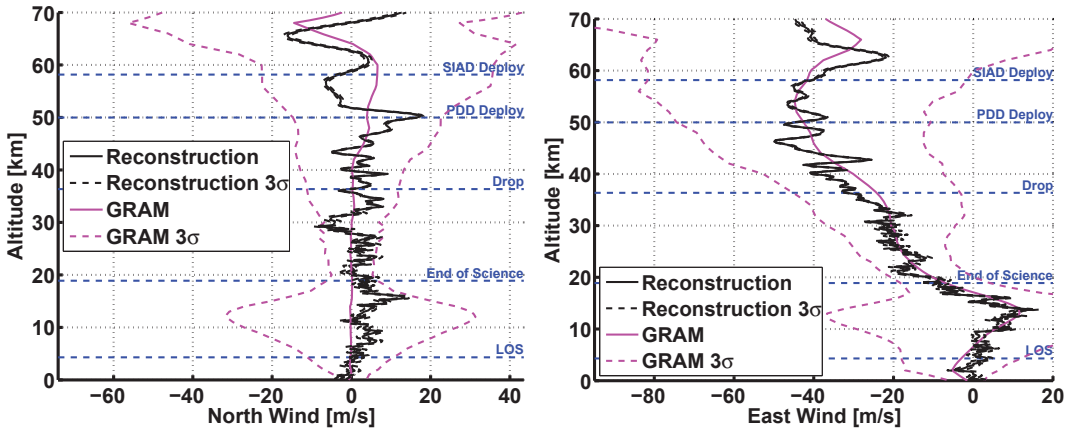

(a) North Wind (b) East Wind

Figure 8: Reconstructed Winds

Reconstructed Trajectory

The test vehicle trajectory was reconstructed from the LN-200 accelerations and angular rates, GPS, and radar measurements following the process described previously. The reconstruction was initialized 60 seconds before test vehicle drop, based on GPS position and velocity. The vehicle attitude was initialized using the GLN-MAC navigation state. Reconstruction of state variables was performed until loss of signal at 858.8 seconds and an altitude of approximately 4300 meters.

The measured GLN-MAC resolver angle and reconstructed mass properties profiles were used to transform the reconstructed LN-200 state to the vehicle CG. The acceleration and angular rate measurements were filtered using the low pass Fourier filter found in the System Identification Program for Aircraft (SIDPAC)[27] analysis tools. Filtering was performed at 10Hz to remove measurement noise and structural vibration. By applying a frequency domain filter, a zero phase-shift filtered signal was obtained.

The GPS data and uncertainties from the Javad output were used from the initial reconstruction time, 60 seconds before drop, until loss of signal. A 10 ms shift in the GPS data was applied in order to synchronize the signal with the GLN-MAC data. Some data editing was performed to take out tracking data from radar that was not physically consistent with the measured vehicle dynamics, as is typically done with post-test trajectory reconstruction.[17] The Radar Q4 track was used from -60 s before drop up to 440 s, and excluded the data between 0 s and 30 s. Radar Q8 data was used from -60 s before drop to 200 s, and Radar Q9 data was used from the drop time to 200 s. Radar measurement biases were included in the state space as solve-for parameters to be estimated in the filter.

The radar and GPS measurement residuals are shown in Figures 9 and 10. The residuals are computed by taking the difference between the measurement observed during flight and the predicted measurement generated by the filter. An inspection of the measurement residuals provides an assessment of the filter performance relative to the measurement uncertainties. Given a perfect estimate of the state and a measurement with no error, the resulting residual value would be zero. Since both situations are nearly impossible, non-zero residual values are observed that largely fall inside of the 3σ uncertainties. Note that specific periods exist where residual values exceed the 3σ bounds. This behavior is most prominent near particular events in the trajectory such as SIAD deployment, PDD deployment and SSDS deployment, where measurement errors can grow due to the vehicle dynamics. In spite of these deviations, the measurement residuals indicate that the state estimates properly reconciled the radar and GPS measurements, and that the filter performed very well. While not shown, the residual results for elevation, geodetic latitude, longitude, east velocity and down velocity are comparable to those shown in Figures 9 and 10.

The reconstructed time histories of geodetic altitude, Mach number and dynamic pressure are shown in Figure 11. Total angle of attack during powered flight and angle of attack and sideslip during SIAD flight are shown in Figure 12.

The most notable off-nominal behavior of the SFDT-1 trajectory was the altitude gained by the TV during powered flight. Compared to the maximum altitude of 52.86 km predicted by the nominal pre-flight simulation, the 61.57 km maximum altitude reached by the vehicle in flight was near the maximum predicted case

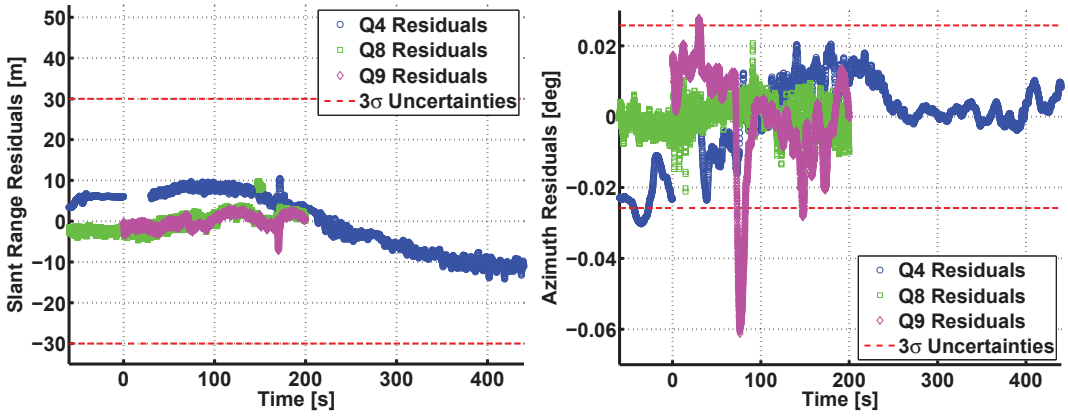

(a) Slant Range Residuals

(b) Azimuth Residuals

Figure 9: Radar Measurement IEKF Residuals

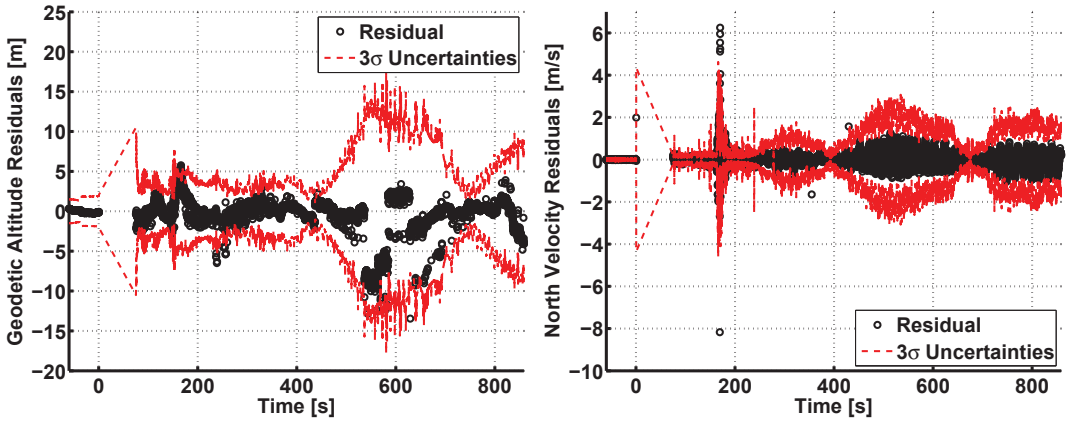

(a) Geodetic Altitude Residuals

(b) North Velocity Residuals

Figure 10: GPS Measurement IEKF Residuals

for all simulations. The most likely contributors to the increased altitude were an over-performance of the STAR-48 motor as well as error in the predicted aerodynamic moment coefficients. These contributors will be described in more detail in the following section. The off-nominal thrust profile also led to a Mach number of 4.32 at burnout, significantly higher than the predicted value of 4.10. In reaching a higher than expected altitude, the TV traveled through a much thinner atmosphere at burnout resulting in a value of dynamic pressure, 623 Pa, that was 33% lower than the predicted value of 973 Pa. A deeper investigation of the pre-flight simulated trajectory as compared to the reconstructed trajectory can be found in Reference 18.

The timing of various events was also affected by the lofted trajectory. Deployment of the SIAD was based on a velocity trigger, and because of the decreased atmospheric density at burnout, the time needed to decelerate the vehicle to the desired velocity during the coast phase was extended from a pre-flight value of 6.18 s to an as-flown time of 11.91 s. Relative to drop, the SIAD was deployed 83 s into the flight as compared to the pre-flight deployment time of 77.39 s. Similarly, in order to reach the targeted velocity for PDD deployment, SIAD flight ended 161.58 s after drop instead of the pre-flight time of 107.97 s. As such, the vehicle flew in a SIAD deployed configuration for 78.58 s, which was 48 s longer than the expected period of 30.58 s.

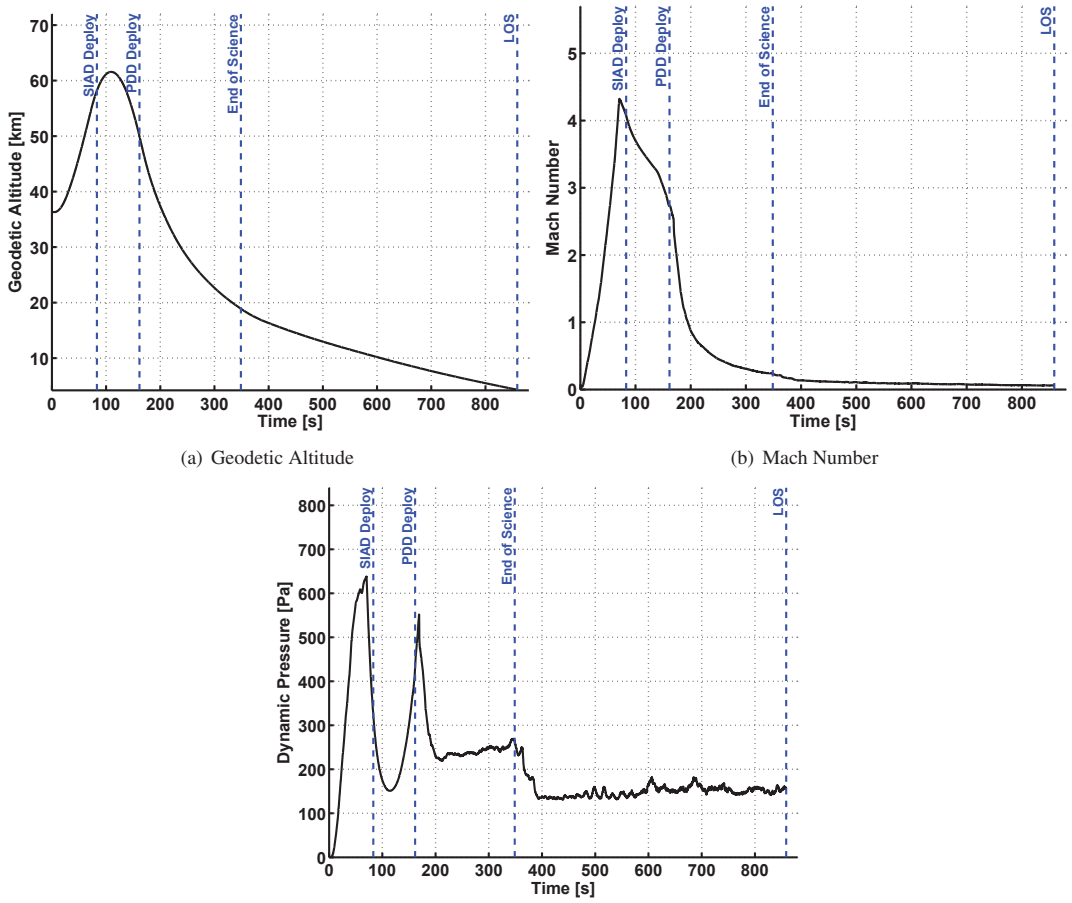

(a) Geodetic Altitude

(b) Mach Number

(c) Dynamic Pressure

Figure 11: Reconstructed Trajectory States

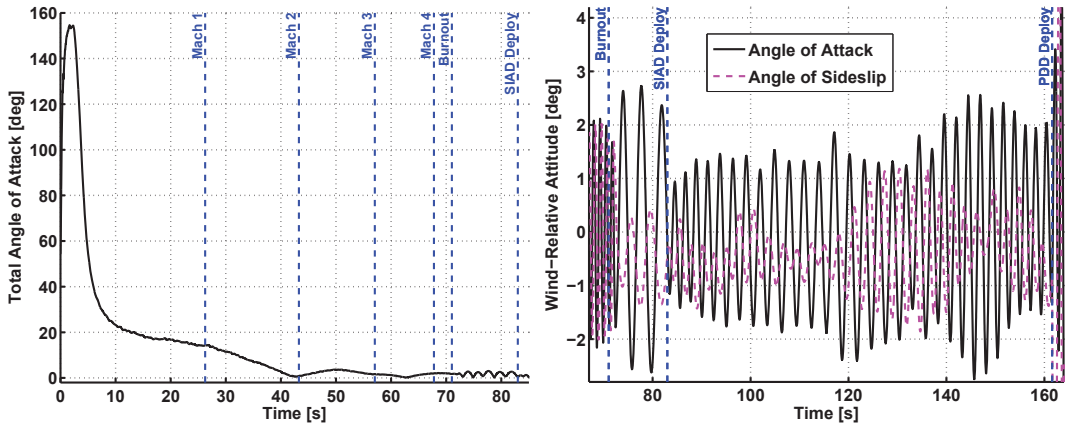

(a) Total Angle of Attack - Powered Flight

(b) Angle of Attack and Sideslip - SIAD Flight

Figure 12: Reconstructed Wind-Relative Attitude

Reconstructed Aerodynamics

The vehicle aerodynamics were reconstructed using the measured accelerations and angular rates with Eqs. (1) and (2). During powered flight, a reconstructed STAR-48 motor burn profile was also needed in

order to separate the thrust forces from the total forces measured by the IMU. Additionally, the reconstructed thrust was required for the flight dynamics and simulation reconciliation effort, due to its high sensitivity in pre-flight modeling and targeting.[21] In order to obtain the STAR-48 thrust profile, a chamber pressure sensor was intended to be utilized during powered flight. Due to an issue with the electrical system, the decision was made to disconnect the sensor, preventing a reconstruction of the thrust profile using flight data. As such, the vehicle drag force could not be separated from the STAR-48 thrust, precluding the reconstruction of powered phase axial force coefficient. Side force, normal force and aerodynamic moments, while still able to be computed during powered flight without a thrust profile, could be corrupted by thrust force misalignment. Thus, due to the lack of information during powered flight, aerodynamics during this portion of the trajectory were not reconstructed.

Although an independent reconstruction was not achievable due to the lack of a chamber pressure measurement, a reasonable alternative used for the simulation reconciliation analysis was to estimate the thrust from the measured accelerations, reconstructed mass properties and wind-relative vehicle states, and the pre-flight aerodatabase. At each instant in time during the powered phase of flight, the aerodatabase was queried at the reconstructed flight condition and the thrust was computed from the sensed acceleration and the predicted aerodynamic forces. Uncertainties in the thrust reconstruction were computed based on the uncertainties in the trajectory reconstruction and uncertainties in the pre-flight aerodatabase.

The results indicated that the STAR-48 produced more thrust early in the profile during subsonic flight. The higher thrust caused the vehicle to climb at a higher flight path angle, which contributed to the vehicle lofting. Other uncertainties in the aerodynamic moments also are likely to have contributed to the vehicle lofting. Detailed reconciliation of pre-flight simulation models during the powered flight phase are described in Reference 18.

The reconstructed profiles of C_A, C_Y and C_m during the SIAD phase (during which time the vehicle flew ballistically), are shown in Figure 13. These profiles are compared to the predicted values, which are obtained by querying the aerodynamic database at the reconstructed flight condition. Additionally, the 3σ uncertainties for both the reconstructed and predicted histories are shown.

The reconstructed time histories of force and moment coefficients during SIAD flight reveal a very strong match to the predicted values. The differences are still within the computed uncertainties, which lends support towards the accuracy of the pre-flight aerodynamic modeling. A slight decrease in C_A of roughly 3%-5% exists between the reconstructed and predicted profiles. This behavior occurs very near peak altitude (109.5 seconds), which suggests a possible deviation in reconstructed density. It should also be noted that the reconstructed C_N and C_n profiles during SIAD flight, while not shown in Figure 13, match the predicted values equally well.

The reconstructed static stability of the TV during the coast and SIAD phases of SFDT-1 is shown in Figure 14. The predicted profile computed from the nominal aerodatabase is also shown. Recall that C_{m_α} is computed by fitting a sine wave to the measured pitch rate of the vehicle, and using the frequency of oscillation of the fitted curve (as shown in Eq. 5) to compute the stability derivative. An example of the fitted pitch rate signal at a point during SIAD phase is shown in Figure 14(b). Because one or two oscillations cycles are required to properly fit the sinusoid, a limited number of points were used to compute C_{m_α}. One point was chosen during the coast phase at Mach 4.2, and three points were chosen during the SIAD phase at Mach 4.0, 3.5 and 3.2. Note that C_{n_β} could not be derived from the flight data using the same methodology, resulting in Eq. 6, because the measured yaw rate did not exhibit an oscillatory signal strong enough to perform the parameter identification analysis.

It is clear from Figure 14(a) that the pre-flight prediction matches the reconstructed value much better during the coast phase than in the SIAD phase. One potential reason for the difference in profiles is in how the aerodatabase was assembled. The computational fluid dynamics code used to populate the aerodatabase[28] was performed at angle of attack values much larger than experienced during SIAD flight. Between these grid points, non-linearities in the C_{m_α} profile likely exist that would not be accounted for by the interpolation schemed used inside of the aerodatabase. Thus, some error would exist in the low angle of attack range seen during SIAD flight due to this lack of fidelity in the aerodatabase. Another factor that could reconcile the reconstructed and aerodatabase curves are the mass and geometric properties used to compute C_{m_α}. A decrease in inertia, an increase in capsule diameter, or a combination of the two could account for some of the discrepancy seen during SIAD flight. However, such errors in inertia and reference area are unlikely considering the small pre-flight uncertainties in these properties.

The pre-flight nominal and reconstructed total angle of attack histories during the inflated SIAD-R segment of the trajectory are plotted in Figure 15. The dynamic stability of the flight vehicle during this phase of the flight can be estimated qualitatively. Note the lofted trajectory of SFDT-1 resulted in a higher initial Mach

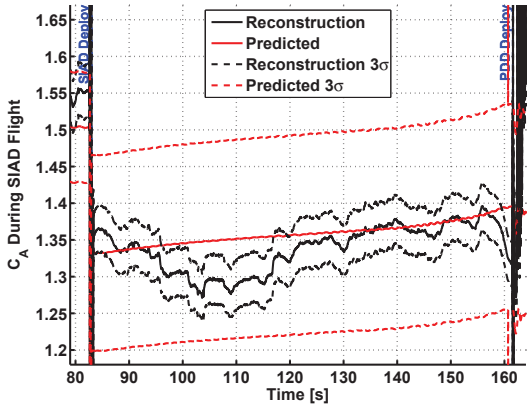

(a) C_A

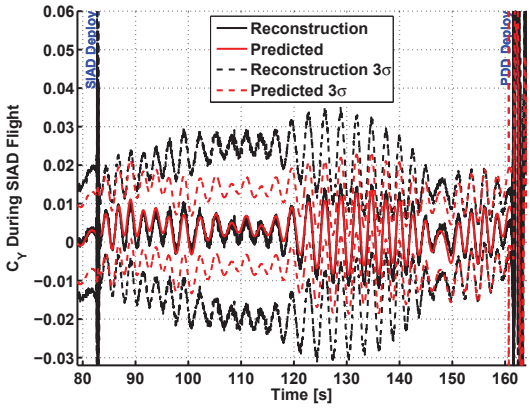

(b) C_Y

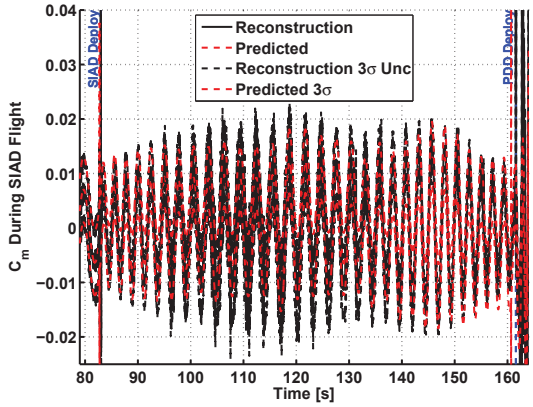

(c) C_m

Figure 13: Reconstructed Aerodynamic States

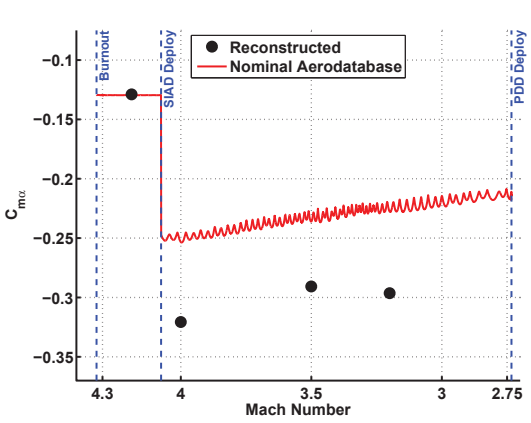

(a) Comparison of Reconstructed and Predicted C_{m_α}

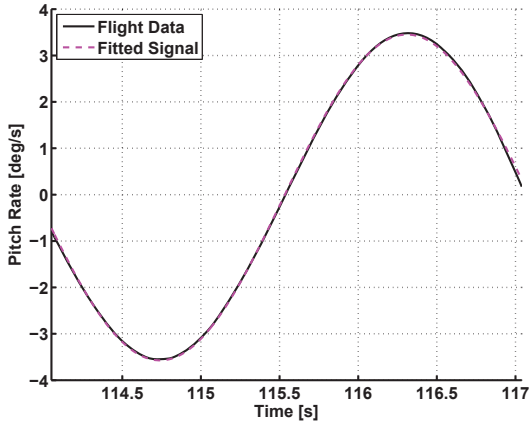

(b) SIAD Phase Point - Mach 3.5

Figure 14: Static Aerodynamic Stability Reconstruction Data

number and longer overall flight time in the SIAD-R configuration. The initial oscillation amplitude was smaller than preflight predictions, but overall the amplitudes and amplitude growth histories are very similar. There is no obvious indication of any significant dynamic instabilities and the preflight model appears to have predicted the vehicle dynamic stability well within the model uncertainties. The density is also plotted

in Figure 15. It shows that the peak altitude of the flight occurred during the SIAD-R phase. At the trajectory apex, density is approximately constant. Therefore, a 10 second segment of the trajectory at the apex was used to extract the pitch-damping coefficient using the angle of attack history.

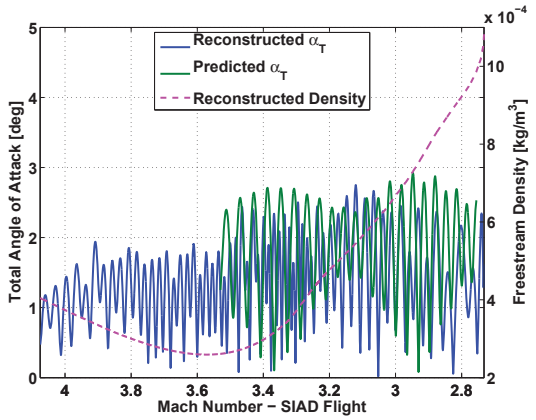

Figure 15: Comparison of Reconstructed and Predicted Total Angle of Attack

A moving window of 5 seconds was used to fit the EC equation to the reconstructed angle of attack history. The mean damping was identified and the window was moved to the next time step and the process was repeated. An example of the curve, fit to the data, is plotted in Figure 16(a). Note that the oscillations are roughly constant in amplitude across this segment of data. The Mach number and freestream density are also plotted to show that both are changing little over this segment of the trajectory. Therefore each solution derived from the curve fit provides a damping coefficient for the same Mach number and amplitude of oscillation. The C_{m_q} points calculated from each curve fit are plotted in Figure 16(b) and compared with the pitch damping model used in the SIAD-R aerodynamic database. The SIAD-R data was measured in a ballistic range test conducted at the Hypersonic Free Flight Aerodynamics Facility (HFFAF) at NASA Ames Research Center.[29]

The data extracted from the SFDT-1 flight have a fairly wide spread. The variation in the C_{m_q} results for each sliding window fit is due to a small amount of interplay between the pitch and sideslip oscillations and a small roll rate. The extra degrees of freedom result in violations of the planar oscillation assumption that produce noise in the C_{m_q} results. However, all of the data points extracted from the SIAD-R trajectory suggest that the pitch damping is more stable at small angles than the ballistic range data indicate. The ballistic range test used to characterize the SIAD-R pitch damping model, recorded very few data points at the small oscillation amplitude at which the SIAD-R was flying. It is not clear whether there is a real difference at small angles between the full-scale vehicle and the rigid ballistic range models, or if the ballistic range results were not sufficiently anchored with low amplitude data.

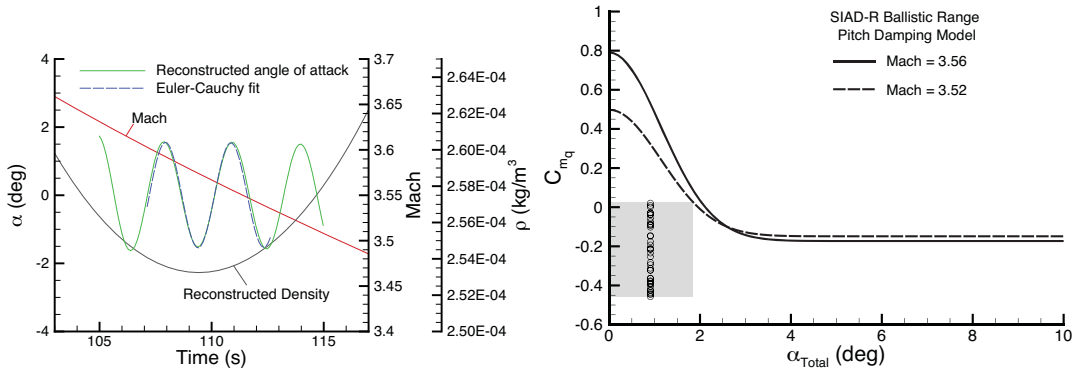

(a) Angle of Attack Curve Fit Data

(b) Comparison of Reconstructed and Predicted C_{m_q}

Figure 16: Dynamic Stability Reconstruction Data

The main finding is that the oscillations were small in amplitude and remained small through the SIAD-R phase of flight. This is consistent with the preflight prediction as shown in Figure 15. The disagreement between the extracted pitch damping and the ballistic range data is likely due to both the limited data at small amplitudes in the ballistic range test and the limiting assumptions of the parameter identification method.

CONCLUSIONS

On June 28th, 2014, the Low Density Supersonic Decelerator project successfully flew a full-scale flight test known as the Supersonic Flight Dynamics Test. This first flight was used to validate the test architecture, including demonstrating powered flight and successful triggering of events. The flight test successfully accomplished these objectives, as well as providing measurements of SIAD and PDD performance. The sensor measurements acquired during the flight test were of good quality, allowing a vehicle trajectory, atmosphere, and aerodynamic reconstruction to be performed. The reconstructed trajectory was a critical input to the post-flight simulation model reconciliation effort. The results of the reconciliation led to several important modeling updates, which will be utilized for pre-flight targeting and launch operations for the future flight tests, scheduled to occur in the summer of 2015.

ACKNOWLEDGEMENTS

The authors are grateful to members of the LDSD reconstruction, flight dynamics, and aerosciences teams, including Jody Davis, Mark Ivanov, Haijun Shen, Scott Striepe, Angela Bowes, Joseph White, and John Van Norman.

NOTATION

$\boldsymbol{a}$	linear acceleration
α	angle of attack
α_T	total angle of attack
β	angle of sideslip
C_A, C_Y, C_N	axial, side, and normal force coefficient
C_l, C_m, C_n	roll, pitch, and yaw moment coefficient
C_{m_α}	Pitch moment static stability derivative
C_{m_q}	Pitch moment dynamic stability derivative
C_{n_β}	Yaw moment static stability derivative
d	reference diameter of test vehicle
$\mathcal{I}$	inertia matrix
$\mathcal{I}_{xx}, \mathcal{I}_{yy}, \mathcal{I}_{zz}$	principle moments of inertia
m	mass of test vehicle
$\boldsymbol{\omega}$	angular rate vector
$\omega_x, \omega_y, \omega_z$	roll, pitch, and yaw rate
Ω_x, Ω_y	frequency of pitch and yaw rate oscillation
q	free stream dynamic pressure
S	reference area of test vehicle
σ	one standard deviation
t	time from test vehicle drop

REFERENCES

[1] Clark, I. G., Adler, M., and Rivellini, T. P., "Development and Testing of a New Family of Supersonic Decelerators," AIAA Paper 2013-1252, March 2013.

[2] Giersch, L., Rivellini, T., Clark, I., Shook, L., Ware, J., and Welch, J., "SIAD-R: A Supersonic Inflatable Aerodynamic Decelerator for Robotic Missions to Mars," AIAA Paper 2013-1327, March 2013.

[3] Coatta, D., Jurewicz, D., Tutt, B., Rivellini, T., and Clark, I., "Development and Testing of an 8 Meter Isotensoid Supersonic Inflatable Aerodynamic Decelerator," AIAA Paper 2013-1328, March 2013.

[4] Gallon, J. C., Clark, I. G., Rivellini, T. P., Adams, D. S., and Witkowski, A., "Low Density Supersonic Decelerator Parachute Decelerator System," AIAA Paper 2013-1329, March 2013.

[5] Cook, B. T., Blando, G., Kennett, A., Von Der Heydt, M., Wolff, J. L., and Yerdon, M., "High Altitude Supersonic Decelerator Test Vehicle," AIAA Paper 2013-1353, March 2013.

[6] Ivanov, M. C., Blood, E. M., Cook, B. T., Giersch, L. R., Grover, M. R., Jakobowski, J. K., Rivellini, T. P., Su, R. P., Samareh, J. A., Zang, T. A., Winski, R. G., Olds, A. D., and Kinney, D. J., "Entry, Descent and Landing Systems Analysis Study: Phase 2 Report on Mars Science Laboratory Improvement," NASA TM-2011-216988, January 2011.

[7] Anon., "NASA Sounding Rocket Program Handbook," Sounding Rockets Program Office, Suborbital and Special Orbital Projects Directorate, Goddard Space Flight Center, Wallops Flight Facility, Wallops Island, Virginia, 810-HB-SRP, June 2005.

[8] Hedin, A. E., "Extension of the MSIS Thermosphere Model into the Middle and Lower Atmosphere," *Journal of Geophysical Research*, Vol. 96, No. A2, 1991, pp. 1159–1172.

[9] Crassidis, J. L. and Junkins, J. L., *Optimal Estimation of Dynamic Systems*, Chapman & Hall/CRC, Boca Raton, FL, 2004.

[10] Wagner, W. E., "Re-Entry Filtering, Prediction, and Smoothing," *Journal of Spacecraft and Rockets*, Vol. 3, No. 9, 1966, pp. 1321–1327.

[11] Wagner, W. E. and Serold, A. C., "Formulation on Statistical Trajectory Estimation Programs," NASA CR-1482, January 1970.

[12] Karlgaard, C. D., Tartabini, P. V., Blanchard, R. C., Kirsch, M., and Toniolo, M. D., "Hyper–X Post–Flight Trajectory Reconstruction," *Journal of Spacecraft and Rockets*, Vol. 43, No. 1, 2006, pp. 105–115.

[13] Karlgaard, C. D., Tartabini, P. V., Martin, J. G., Blanchard, R. C., Kirsch, M., Toniolo, M. D., and Thornblom, M. N., "Statistical Estimation Methods for Trajectory Reconstruction: Application to Hyper-X," NASA TM-2009-215792, August 2009.

[14] Karlgaard, C. D., Beck, R. E., O'Keefe, S. A., Siemers, P. M., White, B. A., Engelund, W. C., and Munk, M. M., "Mars Entry Atmospheric Data System Modeling and Algorithm Development," AIAA Paper 2009-3916, June 2009.

[15] O'Keefe, S. A. and Bose, D. M., "IRVE-II Post-Flight Trajectory Reconstruction," AIAA Paper 2010-7515, August 2010.

[16] Olds, A. D., Beck, R. E., Bose, D. M., White, J. P., Edquist, K. T., Hollis, B. R., Lindell, M. C., Cheatwood, F. M., Gsell, V. T., and Bowden, E. L., "IRVE-3 Post-Flight Reconstruction," AIAA Paper 2013-1390, March 2013.

[17] Karlgaard, C. D., Beck, R. E., Derry, S. D., Brandon, J. M., Starr, B. R., Tartabini, P. V., and Olds, A. D., "Ares I-X Trajectory Reconstruction: Methodology and Results," *Journal of Spacecraft and Rockets*, Vol. 50, No. 3, 2013, pp. 641–661.

[18] Dutta, S., Bowes, A., Striepe, S., Davis, J., Queen, E., Blood, E., and Ivanov, M., "Supersonic Flight Dynamics Test 1 - Post-Flight Assessment of Simulation Performance," AAS Paper 15-219, January 2015.

[19] Karlgaard, C. D., Kutty, P., Schoenenberger, M., Munk, M. M., Little, A., Kuhl, C. A., and Shidner, J., "Mars Science Laboratory Entry Atmospheric Data System Trajectory and Atmosphere Reconstruction," *Journal of Spacecraft and Rockets*, Vol. 51, No. 4, 2014, pp. 1029–1047.

[20] Heck, M. L., Findlay, J. T., Kelly, G. M., and Compton, H. R., "Adaptation of a Strapdown Formulation for Processing Inertial Platform Data," *Journal of Guidance, Control, and Dynamics*, Vol. 7, No. 1, 1984, pp. 15–19.

[21] Bowes, A., Davis, J., Dutta, S., Striepe, S., Ivanov, M., Powell, R., and White, J., "LDSD POST2 Simulation and SFDT-1 Pre-Flight Launch Operations Analyses," AAS Paper 15-232, January 2015.

[22] Schoenenberger, M., Van Norman, J., Karlgaard, C. D., Kutty, P., and Way, D., "Assessment of the Reconstructed Aerodynamics of the Mars Science Laboratory Entry Vehicle," *Journal of Spacecraft and Rockets*, Vol. 51, No. 4, 2014, pp. 1076–1093.

[23] Schoenenberger, M., Kutty, P., Queen, E., and Karlgaard, C., "The Aerodynamics of Axisymmetric Blunt Bodies Flying at Angle of Attack," Paper 2283-2, IEEE Aerospace Conference, Big Sky, MT, March 2014.

[24] Schoenenberger, M., Queen, E. M., and Litton, D., "Oscillation Amplitude Growth for a Decelerating Object with Constant Pitch Damping," AIAA Paper 2006-6148, August 2006.

[25] Leslie, F. W. and Justus, C. G., "The NASA Marshall Space Flight Center Earth Global Reference Atmospheric Model - 2010 Version," NASA TM-2011-216467, June 2011.

[26] Sivakumar, V., Bencherif, H., Hauchecorne, A., Keckhut, P., Rao, D. N., Sharma, S., Chandra, H., Jayaram, A., and Rao, P. B., "Rayleigh Lidar Observations of Double Stratopause Over Three Different Northern Hemisphere Stations," *Atmospheric Chemistry and Physics Discussions*, Vol. 6, 2006, pp. 6933–6956.

[27] Klein, V. and Morelli, E. A., *Aircraft System Identification: Theory and Practice*, AIAA, August 2006.

[28] Muppidi, S., Tang, C., Van Norman, J. W., Bose, D., Clark, I., and Coatta, D., "Aerodynamic Analysis of Next Generation Supersonic Decelerators," AIAA Paper 2014-2990, June 2014.

[29] Yates, Leslie, "Aerodynamic Coefficients from Aeroballistic Range Testing of Deployed and Stowed-SIAD SFDT Models, Final Data Report," Internal LDSD Report, NASA Ames Research Center and AerospaceComputing, Inc., April 2013.